TNF

Technical-Scientific
Faculty

Momentum-dependent Damping for the Rotational Dynamics of Bose–Einstein Condensates

BACHELOR THESIS

for attainment of the academic degree of

Bachelor of Science

in the bachelor study

Technical Physics

Submitted by:
Tina Mitteramskogler

Prepared at:
Institute for Theoretical Physics

Evaluation:
Dr. Robert E. Zillich

Linz, August 2014

Abstract

The time-dependent Gross–Pitaevskii equation (GPE) is numerically solved in the laboratory frame to describe the dynamic behaviour of Bose–Einstein condensates (BECs) such as the dynamics of vortex formation in harmonic traps and the hysteresis of circulation in toroidal BECs. A dissipation mechanism has to be added to the GPE when it is solved numerically, which is usually done via propagating with an imaginary time fraction in the timestep. In this bachelor thesis it is proven that this damping method could not reproduce the experimental results for BECs in harmonic trap, when applied to rotating systems simulated in the laboratory frame instead of the rotating frame of reference. This problem is solved by introducing a momentum-dependent damping model. However, for toroidal condensates, the discrepancy of the critical rotation frequencies between experiments and calculations, which was recently shown by Eckel et al. (S. Eckel et al. "Hysteresis in a quantized superfluid 'atomtronic' circuit". In: Nature 506 (2014), p. 200) was still present.

Contents

1 Introduction

The theoretical prediction of condensation of a dilute quantum gas into the state of lowest energy by Einstein dates back to 1925. Since then many experiments and simulations were performed on liquid helium, rubidium atoms and nowadays on dipolar atoms like Chromium and Dysprosium [1, 2] to create a dipolar Bose–Einstein Condensates (BECs) [3]. By rotating BECs over a critical frequency, vortices with a quantised circulation can be created, which order themselves in lattices when their number increases and the system equilibrates [4, 5, 6].

To simulate the dynamics of BECs with the Gross–Pitaevksii equation (GPE) an additional damping mechanism is used. The BEC is usually damped by introducing an imaginary component to the equation [7, 2]. However, this bachelor thesis shows, that for BECs that are simulated in the laboratory reference frame, this damping model (which we refer to as model A) yields wrong results. We introduce an improved damping model, based on a momentum-dependent damping rate (model B).

In the second chapter, a short overview of the mean field description of the many-body Schrödinger equation that leads to the GPE is given in order to introduce the occurring quantities. In chapter 3, the quadrupole mode and the scissors mode, that can be found in rotating BECs are introduced briefly. The theoretical background of vortices in stirred BECs is shown and the critical rotational frequency for which vortices occur is given in Thomas–Fermi approximation.

To simulate the GPE, second order operator splitting was used. The theory behind this propagation method is derived for time-independent linear Hamiltonians and then generalised to the GPE in chapter 4. It is shown that, by propagating the equation in imaginary time, the ground state of the BEC can be found.

Next, damping model A, that is widely used, and our damping model B are introduced and discussed. These models are tested on the experiment on a rotating BEC in a harmonic trap that Madison et al. performed in 2001 [5] in chapter 5. The damping strength of these two models is compared and a rule of thumb of how to choose the parameters of damping model B is stated.

Then, the dynamics of vortex creation is shown on the basis of two examples. The critical frequency is investigated and some of the occurring modes are interpreted briefly.

In chapter 6, the experiment of Eckel et al. [8], that showed a hysteresis behaviour in the critical rotation frequencies of toroidal BECs, was used as a starting point. They found out that the results for the critical frequencies using the GPE with damping model A differs from the experimental results. We performed simulations on the critical frequencies with damping models A and B to test, whether damping model B yielded better results. However, the results for the critical frequencies with both damping models were the same, so that it can be concluded that damping model B could not resolve the problem described by Eckel et al.

2   The Gross–Pitaevskii Equation

An useful equation to describe the dynamics of a Bose–Einstein condensate (BEC) was found by Eugene P. Gross and Lev Pitaevskii in 1961 [9, 10]. In the following section, a short overview of their approach shall be given in order to define the quantities that will be of later use. When the temperature in a low density Bose gas is close to zero Kelvin, the effective interaction between atoms can be modelled as

$$\tilde{V}_{int}(\mathbf{k}) = \frac{4\pi\hbar^2 a}{m} \tag{1}$$

in momentum space with a being the s-wave scattering length of atoms with mass m. The Fourier transform of this potential results in the corresponding real space interaction

$$V_{int}(\mathbf{r} - \mathbf{r}') = g\,\delta(\mathbf{r} - \mathbf{r}') \tag{2}$$

which is depending on the coupling constant $g = N\,4\pi\hbar^2 a/m$ and the positions of the interacting particles $\mathbf{r}$ and $\mathbf{r}'$. By inserting this potential into the N-particle Schrödinger equation and using a mean-field approximation the Gross–Pitaevskii equation (GPE) can be obtained [11]:

$$\left(-\frac{\hbar^2}{2m}\nabla^2 + V(\mathbf{r}) + g\,|\psi(\mathbf{r})|^2\right)\psi(\mathbf{r}) = \mu\,\psi(\mathbf{r}) \tag{3}$$

with normalisation

$$\int |\psi(\mathbf{r})|^2\,\mathrm{d}\mathbf{r} = 1. \tag{4}$$

Here $V(\mathbf{r})$ is an external potential, such as the trap holding the condensate. The GPE can be interpreted as a nonlinear 1-body Schrödinger equation with an additional density dependent repulsive or attractive interaction term $V_g(\mathbf{r}) = g|\psi(\mathbf{r})|^2$.

Yet, in contrast to the Schrödinger equation, its eigenvalue is not the energy but chemical potential μ. Due to the mean-field approximation only two-particle interactions are considered, which is a good approximation for condensates at low temperatures.

3 Rotating Condensates

Suppose a BEC is initially in the ground state of an asymmetric two dimensional trap with frequencies w_x and w_y along the $\hat{x}$- and $\hat{y}$-axis respectively. A sudden rotation of the trap with frequency Ω excites higher modes of the condensate and the condensate will start to oscillate. In order to describe this oscillatory behaviour it is convenient to introduce the distortion parameter [12]

$$\alpha \equiv -\Omega \frac{\langle y^2 - x^2 \rangle}{\langle y^2 + x^2 \rangle} \tag{5}$$

and the deformation of the trap

$$\varepsilon \equiv \frac{\omega_x^2 - \omega_y^2}{\omega_x^2 + \omega_y^2}. \tag{6}$$

3.1 Quadrupole Mode

Consider a BEC in a trap with $\omega_\perp = \omega_x = \omega_y \neq \omega_z$. The energy of the excited modes can be obtained analytically when the kinetic energy term in equation (3) is neglected. This approximation is the Thomas–Fermi limit of the GPE, which holds for large g or a large number of particles. One mode that is of special interest is the quadrupole mode with its solutions [3]:

$$\omega^2(l = 2, m = \pm 2) = 2\,\omega_\perp^2 \tag{7}$$

$$\omega^2(l = 2, m = \pm 1) = 2\,\omega_\perp^2 + \omega_z^2. \tag{8}$$

3.2 Scissors Mode

Another mode that can be observed in rotating condensates is the scissors mode. It is the oscillatory behaviour of a trapped condensate that occurs when the main axis of the potential is shifted abruptly. The result is an oscillation of α and the angle between the main axis of the potential and the main axis of the condensate with equal frequencies [13]. It has been shown that the scissors mode cannot only be excited by a sudden shift of the potential, but also by a constant rotation of the condensate, i.e. a rotation of the main axis of the condensate with frequency $\Omega \geq \omega_\perp/\sqrt{2}$ [12]. By assuming a small trap deformation $\varepsilon \ll 1$ and a constant Ω, the frequency of this oscillatory mode is given by [13]:

$$\omega_{sc} = \sqrt{\omega_x^2 + \omega_y^2}. \tag{9}$$

3.3 Vortices

From the hydrodynamic equations that follow from the GPE in the Thomas–Fermi limit it can be shown that the integral over the velocity field $\mathbf{v}$ around a closed loop is given by [3]

$$\oint \mathbf{v}\, d\mathbf{l} = 2\pi\, l \frac{\hbar}{m} \tag{10}$$

with l being an integer number. This quantisation accounts for the existence of vortices with quantised circulation, which are defined as points where $l \neq 0$.

The distance at which a BEC regains its bulk value when a hard wall perturbs it is defined as the healing length

$$\xi = \frac{\hbar}{\sqrt{2\, m\, g\, n}} \tag{11}$$

with n being the bulk density. The healing length can be used to estimate the size of a vortex core.

In the case of two dimensional condensates with $\omega_x = \omega_y = \omega_\perp$ vortical solutions are of lower energy if the angular velocity of the condensate is larger than the critical velocity in Thomas-Fermi approximation [14]

$$\Omega_{TF} = \frac{\hbar\, \omega_\perp^2}{\mu} \ln\left(\frac{1.776\, \mu}{\hbar\, \omega_\perp} \right). \tag{12}$$

4 Numerical Methods

4.1 Second Order Operator Splitting

The time-dependent GPE

$$i\hbar \frac{\partial}{\partial t}\psi(t) = \hat{H}(t)\psi(t) \tag{13}$$

is used to get the time evolution of the wave function of the condensate. Here $\hat{H}(t) = \hat{V}(t) + \hat{T}$ can be decomposed into a kinetic term and a time dependent potential term. For a time independent Hamiltonian the time evolution can be written as

$$\psi(t + \Delta t) = e^{-\frac{i}{\hbar}\Delta t \hat{H}}\psi(t). \tag{14}$$

In this case the second order factorisation of the exponential is straight forward

$$\psi(t + \Delta t) = e^{-\frac{i}{\hbar}\frac{\Delta t}{2}\hat{V}}e^{-\frac{i}{\hbar}\Delta t \hat{T}}e^{-\frac{i}{\hbar}\frac{\Delta t}{2}\hat{V}}\psi(t) + \mathcal{O}(\Delta t^3). \tag{15}$$

However, the GPE contains a time dependent potential

$$\hat{V}\psi(\mathbf{r},t) = \hat{V}(t)\psi(\mathbf{r},t) = \left(\hat{V}_{ext}(\mathbf{r},t) + g\,|\psi(\mathbf{r},t)|^2\right)\psi(\mathbf{r},t). \tag{16}$$

This time dependency requires the inclusion of the forward time derivative operator $\hat{D} = \overleftarrow{\frac{\partial}{\partial t}}$ which acts to the left as indicated by the arrow [15].

$$\psi(t + \Delta t) = e^{-\frac{i}{\hbar}\Delta t\left(\hat{H}(t) + \hat{D}\right)}\psi(t). \tag{17}$$

It has been shown that in this case the second order operator splitting gives

$$\psi(t + \Delta t) = e^{-\frac{i}{\hbar}\frac{\Delta t}{2}\hat{V}(t+\Delta t)}\,e^{-\frac{i}{\hbar}\Delta t \hat{T}}e^{-\frac{i}{\hbar}\frac{\Delta t}{2}\hat{V}(t)}\psi(t) + \mathcal{O}(\Delta t^3). \tag{18}$$

The potential $\hat{V}(t+\Delta t)$ in equation (16) depends on $\psi(t+\Delta t)$. This implies that for the wave function to be propagated from $\psi(t)$ to $\psi(t+\Delta T)$ the later term would have to be known already.

Fortunately, Chin [16] showed that the part of $\hat{V}(t)$ can be evaluated after the first two exponential operators in equation (18) acted on the wave function. This means that

$$\psi(t + \Delta t) = e^{-\frac{i}{\hbar}\frac{\Delta t}{2}\left(\hat{V}_{ext}(\mathbf{r},t) + g\,|\phi|^2\right)}\underbrace{e^{-\frac{i}{\hbar}\Delta t \hat{T}}e^{-\frac{i}{\hbar}\frac{\Delta t}{2}\left(\hat{V}_{ext}(\mathbf{r},t) + g\,|\psi(\mathbf{r},t)|^2\right)}\psi(t)}_{\phi} + \mathcal{O}(\Delta t^3) \tag{19}$$

yields the correct time evolution up to second order.

As a conclusion, the condensate can be propagated in real time by applying equation (19) consecutively.

4.2   Imaginary Time Propagation

In order to find the ground state wave function of the condensate the method of choice is imaginary time propagation. In the following the Hamiltonian with eigenstates ϕ_n and eigenenergies E_n is assumed to be time independent and linear. In the case of the GPE this method is still applicable, as shown by Chiofalo et al. in 2000 [17].
By substituting

$$\mathrm{i}\,\Delta t \;\to\; \Delta\tilde{t} \tag{20}$$

in equation (14) one obtains

$$\psi(\Delta\tilde{t}) = e^{-\frac{1}{\hbar}\,\Delta\tilde{t}\,\hat{\mathrm{H}}}\psi(0) \tag{21}$$

at $t = 0$. The wave function can be written in the eigenstates of the Hamiltonian $\psi(0) = \sum\limits_{n} c_n\,\phi_n$ with the result

$$\psi(\Delta\tilde{t}) = e^{-\frac{1}{\hbar}\,\Delta\tilde{t}\,\hat{\mathrm{H}}}\sum_{n} c_n\,\phi_n \tag{22}$$

$$= \sum_{n} e^{-\frac{1}{\hbar}\,\Delta\tilde{t}\,E_n}c_n\,\phi_n. \tag{23}$$

The last equation shows that propagation with imaginary time yields an exponential damping of the eigenstates with a strength proportional to the energy. This means, that by applying this operator consecutively the wave function will be propagated towards the ground state.

4.3   Damping methods

To get a suitable description of the real time behaviour, a damping mechanism has to be introduced to equation (19). It simulates the loss of energy due to interaction with non condensed particles.

In the experiment, a stirring potential excites higher modes of the condensate which collapse into steady vortical states within a timespan depending on the temperature [5]. Without losses, the condensate would never show stable vortex lattices, because they

correspond to local minimas in the energy. This motivates the integration of a damping mechanism.

4.3.1   Model A: Imaginary Time Damping

The easiest choice is to add a small phenomenological dissipation parameter γ to equation (13):

$$i\hbar \frac{\partial}{\partial t} \psi(t) = (1 - i\gamma_A)\hat{H}(t)\psi(t) \tag{24}$$

$$i\hbar \frac{\partial}{\partial t(1 - i\gamma_A)} \psi(t) = \hat{H}(t)\psi(t). \tag{25}$$

It can be seen, that this damping method corresponds to a propagation with a complex time step $t' = t(1 - i\gamma_A)$. Therefore, every real time step the system is simultaneously damped with imaginary time propagation. Hence, this damping method will hereinafter be referred to as "Model A".

Imaginary time damping was first introduced as phenomenological dissipation by Choi in 1998 [18]. When solving the GPE the parameter γ_A is set to a value such that the damping is comparable to experiments (≈ 0.01).

A downside of this damping method is that the damping depends on the exact form $\hat{H}$. It will always propagate towards the state of lowest energy of $\hat{H}$ when the damping parameter γ_A is large enough or when the number of time steps is large. Since damping is introduced by the additional term $-i\gamma_A \hat{H}(t)$, the damping depends on the exact form of $\hat{H}$. That means, that the choice of reference frame strongly influences the damping behaviour.

If we assume a BEC confined in a harmonic trap that rotates with $\Omega > \Omega_{TF}$, a finite ε is needed to generate vortices in experiments, because a rotationally invariant potential can not excite the condensate. However, when solving the GPE in the rotating frame of reference even a however small ε will generate vortices using imaginary damping, which is physically impossible. However, this damping method is widely used in the GPE term [7, 2, 8].

4.3.2   Model B: k-dependent Damping

A solution to the problem of $\hat{H}$ dependent damping can be found by introducing a dissipation that only depends on the momentum k instead of $\hat{H}$. The simplest case is to

damp momenta that are greater than a certain value k_0, which yields

$$i\,\hbar\,\frac{\partial}{\partial t}\,\psi(t) = \left(\hat{H}(t) - i\,\gamma_B\,\Theta(k - k_0)\right)\psi(t) \tag{26}$$

where $\Theta(k - k_0))$ is the Heaviside function. In the experiment, this would correspond to particles with large momenta evaporating from the condensate. The parameter γ_B is used to define the damping strength, whereas k_0 linked to the healing length of the setup:

$$k_0 = \frac{2\,\pi}{n\,\xi}. \tag{27}$$

A value of $n \approx 6$ yields best results. A too large k_0 will not provide enough damping, whereas a too small n will influence the system too much, because even the ground state will be affected by damping.

In principle, any function can be used in place of $\Theta(k - k_0))$. A smooth approximation to the step function, like $1/2\,(1 + \tanh(s\,k))$, with s being the steepness, yields more stable vortex lattices, because also smaller k-values are damped slightly.

This damping method will be referred to as "Model B".

5 Bose–Einstein Condensates in a Rotating Trap

5.1 Reduced Units

In the following, the results for simulations of BECs in rotating traps using either damping model A or B will be illustrated. It is convenient to introduce reduced units depending on the mass of the atoms m, the mean trap frequency $\omega_\perp$ and the oscillator length $x_0 = \sqrt{\hbar/m\,\omega_\perp}$:

$$x' = x/x_0 \tag{28}$$

$$E' = E/\left(\hbar\,\omega_\perp\right) \tag{29}$$

$$\omega' = \omega/\omega_\perp \tag{30}$$

$$g' = g/\left(\frac{\hbar^2}{m}x_0\right) \tag{31}$$

The prime marking the reduced units will be omitted from now on, so that the new GPE gets

$$\left(-\frac{1}{2}\nabla^2 + V(\mathbf{r},t) + 4\pi\,a\,N\,|\psi(\mathbf{r},t)|^2\right)\psi(\mathbf{r},t) = \mathrm{i}\frac{\partial}{\partial t}\,\psi(\mathbf{r},t) \tag{32}$$

with all remaining quantities given in reduced units. Additionally, the period of one full rotation of the external potential $\tau = 2\pi/\Omega$ will be used as time scale.

5.2 Two Dimensional GPE

Condensates that are very weakly confined in the $\hat{z}$-direction can be approximated to be uniform in that direction, which may allow a 2D analysis.

In order to simulate a system with N particles in a cylinder of length L_z with $\omega_z = 0$ and finite $\omega_{x,y}$, the coupling constant is modified [3]

$$g_{3D} \mapsto g_{3D}/L_z \equiv g_{2D}. \tag{33}$$

However, for traps with finite ω_z, a 3D simulation is used to calculate the line density $n(z)$ at position $z = 0$. To get to the corresponding 2D simulation, the line density is assumed to be constant $n(z) = n(0) = N/L_z$, which yields an approximate value for L_z [3].

5.3 Experiment of Madison et al.

This section will show how the two different damping methods affect the dynamic behaviour of a simulated BEC confined in a rotating trap with small deformation.

In 2001 Madison et al. investigated the dynamics of vortex nucleation experimentally by preparing a BEC in the ground state of a deformed harmonic trap and suddenly starting to rotate the condensate [5]. The experiment was done with 3×10^5 ^{87}Rb atoms in a trap with mean frequency $\omega_\perp = 200\,\text{Hz}$ and a small trap deformation $\varepsilon = 0.025$. The ratio between the trap frequencies $\hat{z}$-direction was $\omega_\perp/\omega_z = 9.2$. After equilibration of the BEC in the trap, the rotational frequency Ω was turned on rapidly within $20\,\text{ms}$ ($\approx 1.5\tau$) to a final value of $0.7\omega_\perp$ and held constant afterwards.

The time evolution of the absolute of the distortion parameter can be seen in figure 1. In the first $300\,\text{ms}$ ($\approx 40\tau$) the distortion parameter α oscillates, which corresponds to the oscillating elliptical shape of the condensate. Thereafter a spontaneous decrease of α to a value smaller than 0.1 was observed when vortices enter the condensate and the oscillations of α cease.

It took the BEC about $600\,\text{ms}$ ($\approx 85\tau$) to equilibrate to a stable vortex lattice consisting of 7 vortices. The equilibration time depended on the temperature of the BEC. More precisely, a higher temperature, which corresponds to higher damping in the simulation, led much faster to stable vortex lattices than lower temperatures. However, high temperature also hindered ellipticity of the BEC which is crucial for the onset of vortices.
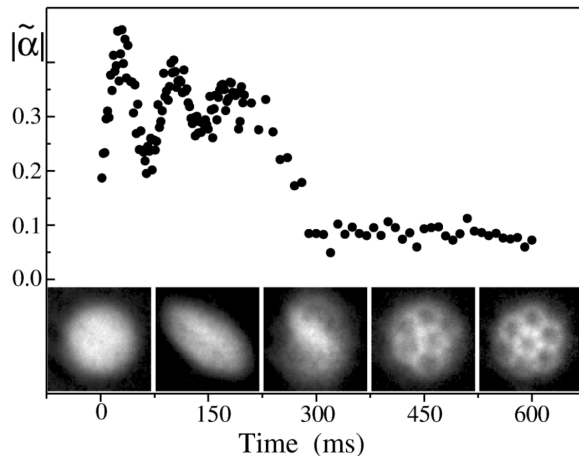
Figure 1: Disortion parameter and density plots for a condensate consisting of 3×10^5 ^{87}Rb atoms in a trap with mean frequency $\omega = 200\,\text{Hz}$ and $\varepsilon = 0.025$. The stirring frequency was turned on rapidly ($20\,\text{ms}$) and held constant for ($300\,\text{ms}$). The experiment showed an oscillation of α followed by the onset of vortices after about 40 rotations ($300\,\text{ms}$). Within 85 rotations ($600\,\text{ms}$) they achieved a stable vortex lattice consisting of 7 vortices. Image taken from reference [5].

5.3.1 Simulation Parameters

The experiment of Madison et al. was simulated with both imaginary and k-dependent damping using the same g, ε, N and Ω in order to be comparable. To ease the onset of vortices, a slightly higher deformation of the trap $\varepsilon = 0.0975$ than in the experiment of Madison et al. was chosen.

A 3D simulation was performed in advance to get the 2D coupling constant $g_{2D} = 252$.

The external potential had the form

$$\hat{V}_{ext}(\mathbf{r}, t) = \frac{1}{2} \left((1 + \varepsilon)\, \tilde{x}^2 + (1 - \varepsilon)\, \tilde{y}^2 \right) \tag{34}$$

with $\tilde{x} = x \cos(\Omega t) - y \sin(\Omega t)$ and $\tilde{y} = x \sin(\Omega t) + y \cos(\Omega t)$.

First, 500 imaginary time steps were performed without rotation of the potential in order to propagate a Gaussian trial function to the ground state of the trap. Then the ground state wave function was propagated in real time with linearly increasing Ω. Within 3τ The rotation frequency arrived the final value of $\Omega = 0.7$.

5.3.2 Damping Model A

The experiment of Madison et al. was simulated with damping model A with $\gamma_A = 0.01$. This value was chosen like in the simulations by Tsubota et al. , who worked in the rotating frame of reference [7].

By damping the simulation with an imaginary part in the time step as described in equation (25), the simulation of the experiment of Madison et al. resulted in no vortices. After 20 rotations of the trap a stable state without vortices was reached, which can be seen in figure 2. The final shape of the condensate was elliptical like the plot corresponding to $t = 150\,\text{ms}$ in figure 1, but further time propagation did not lead to a vortex state.

Figure 3 shows the fast equilibration of the angular momentum. The oscillations in the first few rotations correspond to surface excitations, that would have been necessary to stimulate the creation of vortices. However, these excitations were damped before a vortex could arise. The necessity of these quadrupole excitations for the onset of vortices was experimentally proven [4].
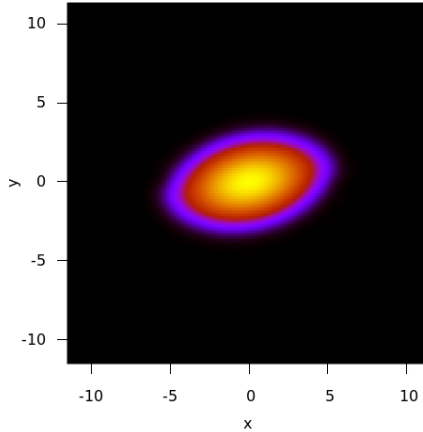
Figure 2: Density of a 2D simulation with time step $\Delta t = 0.005$, $g_{2D} = 252$, $N = 3 \times 10^5$, $\omega_x = 0.95$ and $\varepsilon = 0.0975$ after 20 rotations with $\Omega = 0.7$. The frequency was turned on linearly in the first three full rotations of the potential and held constant afterwards. These parameters were chosen to be comparable with the experiment of Madison et al. [5], yet a higher ε was used to ease the creation of vortices. Even though the experiment resulted in a vortex lattice consisting of 7 vortices, the simulation with damping model A using $\gamma_A = 0.01$ did not yield any vortices.
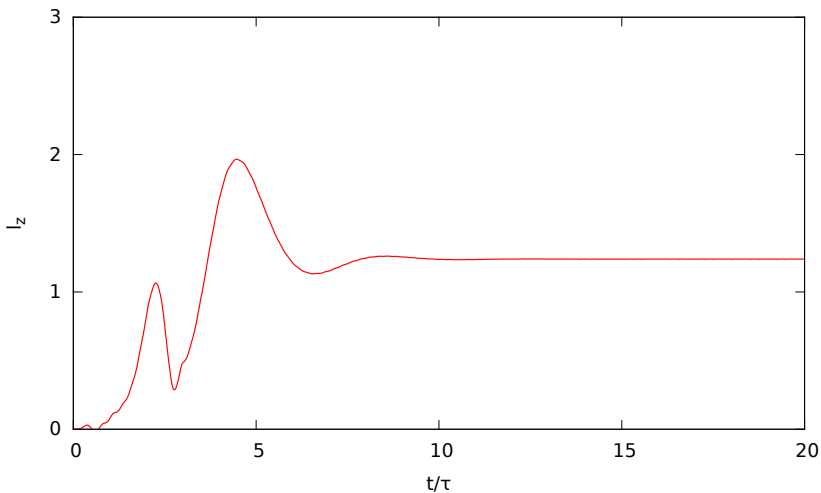
Figure 3: Angular momentum of the simulation with parameters described in figure 2. This plot illustrates the equilibration of the system within 10 rotations. In comparison with Madison et al. the system did not show a spontaneous onset of vortices even within 200 rotations.

5.3.3   Damping Model B

The second damping method we use to simulate the experiment of Madison et al. was model B. The parameters were kept the same as in figure 2, but damping was introduced as described in equation (26). Figure 4 compares the absolute of the Fourier transform of the ground state wave function in red to the damping potential. It can be seen that a choice of $k_0 = 5$ as advocated in equation (27) hardly affects the wave function, because it only damps fast oscillations in k-space.
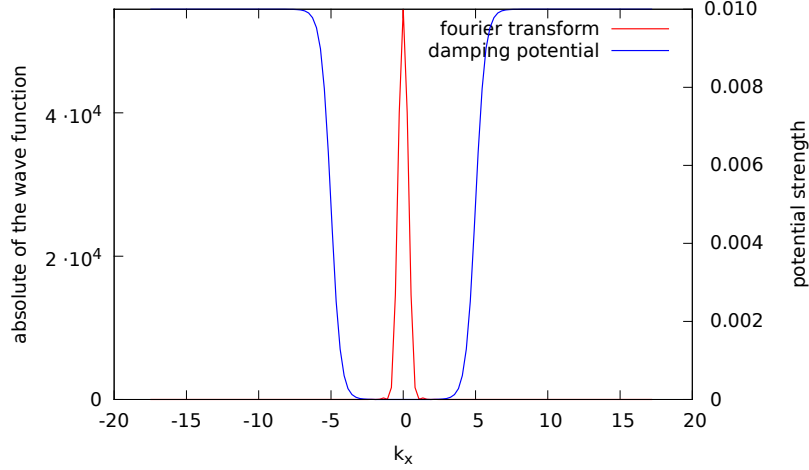
Figure 4: Absolute of the Fourier transform of the ground state wave function obtained with imaginary time propagation (red) and the damping potential of damping model B (blue). Same parameters as in figure 2. It can be seen that $k_0 = 5$ was chosen such that the potential hardly affected the ground state.

The time evolution of the density of the wave function can be seen in figure 5. It shows that in the beginning the shape of the condensate was deformed elliptically due to the quadrupole excitations until vortices started to collocate at the edges of the condensate after $t = 10\tau$. The elliptical shape of the condensate was lost after the first vortex had entered the condensate from the border of the BEC. After 200 rotations a stationary vortex lattice as in the experiment of Madison et al. was created.

Figure 6 shows the corresponding phase map to figure 5. It can be seen how the positions of the phase jumps moved closer and closer to the edges of the condensate until one entered the condensate spontaneously as a vortex.
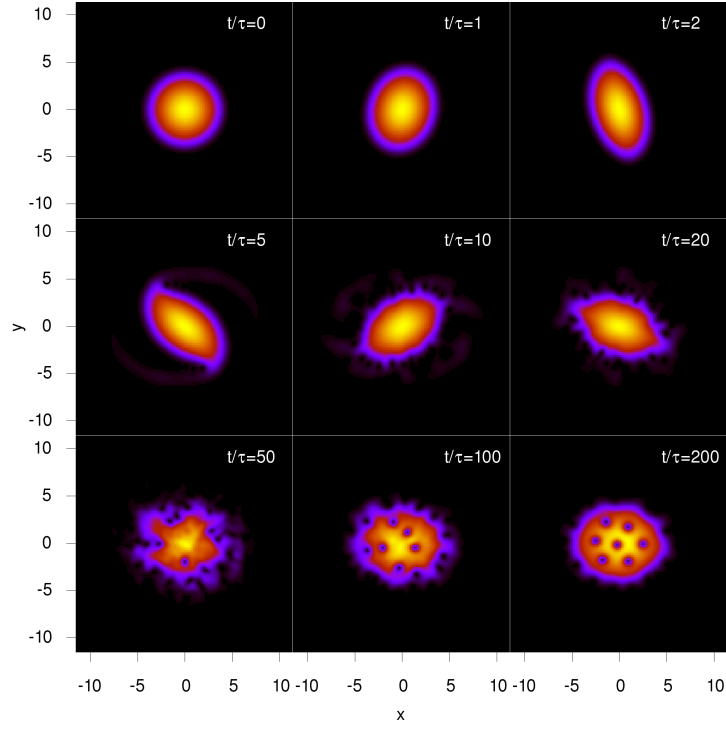
Figure 5: Time evolution of the density of the wave function using damping model B. The parameters were: $\Delta t = 0.005$, $g_{2D} = 252$, $N = 3 \times 10^5$, $\omega_x = 0.95$ and $\varepsilon = 0.0975$. The parameters of the damping model were $k_0 = 5$ and $\gamma_B = 0.01$ The spontaneous onset of vortices can be seen after about 50 rotations when vortices entered from the border in accordance with the experiment by Madison et al. However, it took longer for the system until the vortex lattice stabilised (200 rotations in the simulation compared to 84 in the experiment).
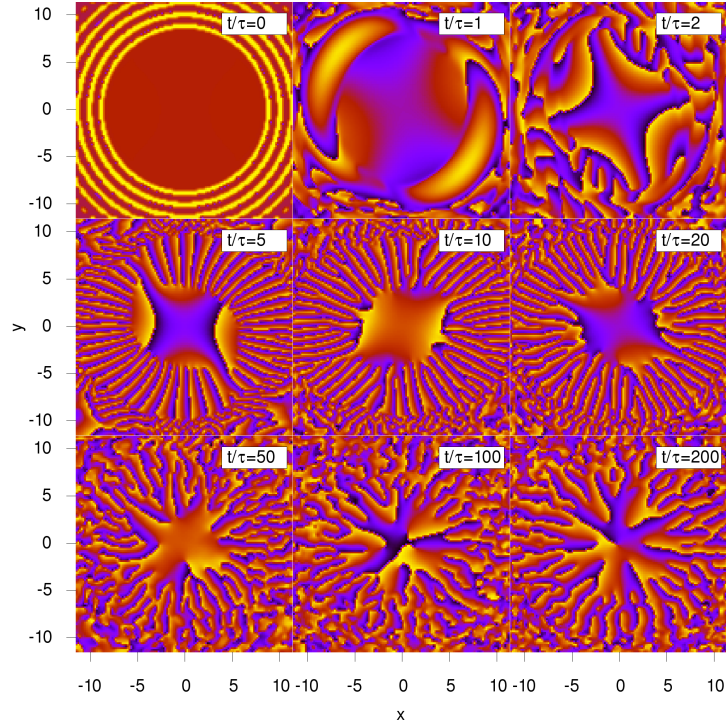
Figure 6: The corresponding phase map of figure 5. It shows how vortices order along the borders of the condensate, before the first vortex enters.

14

Greater insight into the system is gained by looking at the time dependency of the angular momentum in figure 7. The oscillation in the first few rotations is a sign of the scissors mode. The spontaneous increase of the angular momentum after 50 rotations was caused by a vortex entering the condensate. Even though the vortices enter the condensate relatively fast, full equilibration of the angular momentum takes much longer.
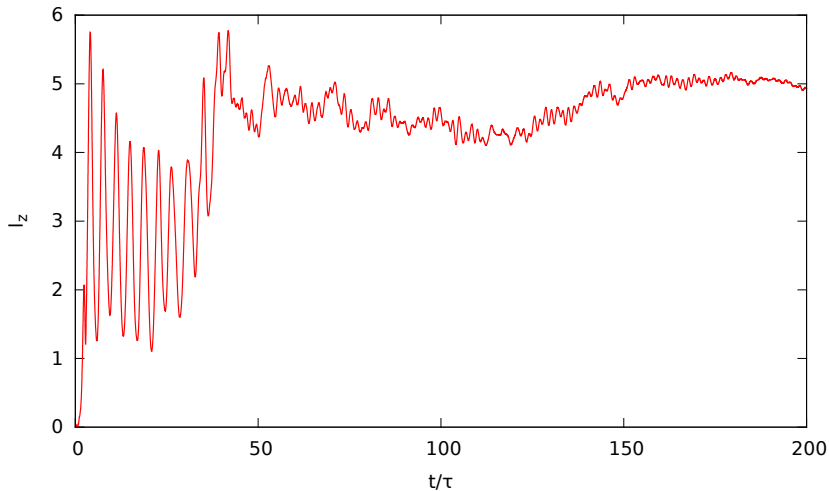
Figure 7: Angular momentum of the simulation described in figure 5. First, the angular momentum showed oscillations that corresponds to quadrupole excitations until the first vortex entered the condensate after 50 rotations. When the vortex lattice was ordered, the angular momentum stabilised.

As it has been done in the experiment by Madison et al., the disortion parameter was calculated and plotted in figure 8. The same oscillations in the distortion parameter were observed, even though the first vortex enters the condensate about 10 rotations later than in the experiment. The vanishing of fluctuations is again an indication that a stationary vortex lattice was reached. The final value of α of ≈ 0.13 was higher than in the experiment ($\alpha \approx 0.07$), due to the greater ε.

To demonstrate that the oscillations in α are caused by the scissors mode, the frequency was fitted to a sine function (figure 8). The estimated frequency of this oscillation was $\omega_\alpha = 1.664 \pm 0.003$, whereas the expected scissors mode frequency in the Thomas–Fermi limit is $\omega_{sc} = 1.414$ according to equation (9). However, the approximation of neglecting the kinetic energy may not hold in this case due to a relatively small g.

15
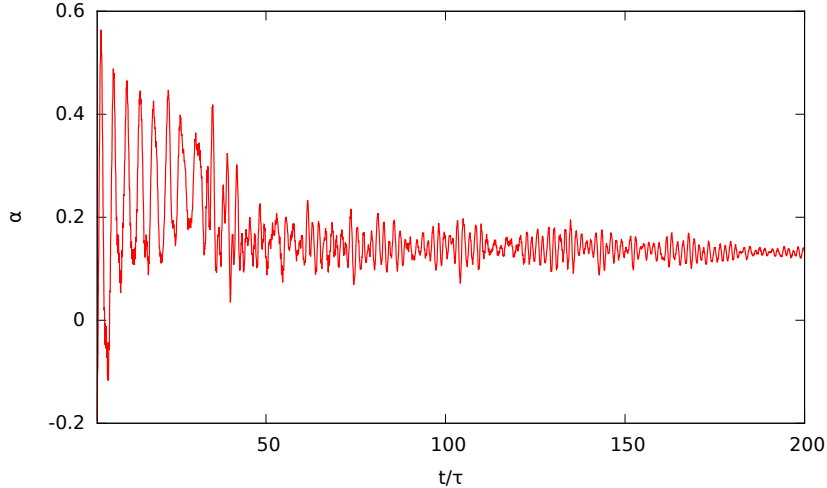
Figure 8: Distortion parameter α of the simulation described in figure 5. First, the quadrupole modes were excited that lead to the sinusoidal behaviour in the first 30 rotations. Afterwards, when the vortices entered the condensate, the system lost its deformed shape and the distortion parameter stabilised around $\alpha = 0.13$ which is a bit higher than in the experiment where it converged to a value less than 0.10.
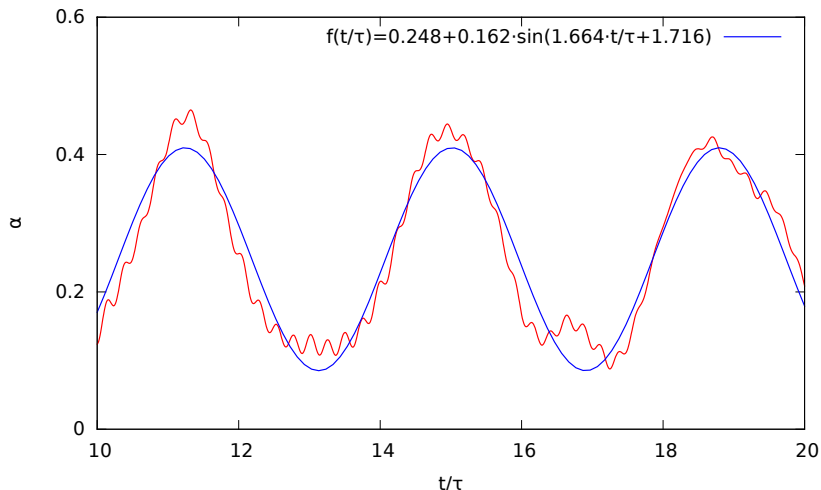
Figure 9: Distortion parameter as in figure 8. This plot shows the quadrupole oscillations in the first few rotations fitted with a sine function.

5.3.4 Comparison of Damping Strength

In order to compare the strength of the damping potential for the two previously mentioned simulations, a simulation was performed where a change in the number of particles due to damping was allowed by not renormalising the wave function. The parameters g, ε and N were chosen exactly the same as mentioned in section 5.3.1, but without rotating the potential.

For both damping models a decrease of the number of particles can be seen. The simulation with damping model B lost 0.0077% of the particles within 200 rotations, whereas

with damping model A more than 50% were lost.

To get comparable losses a extremely low γ_A between 1×10^{-9} and 2×10^{-9} was needed for imaginary damping. However, that little damping was not able to hinder the condensate from showing instabilities, which can be seen by the increasing energy shown in figure 10. Here, the energy of the simulation with $\gamma_A = 2 \times 10^{-9}$ is compared to the energy corresponding to the simulation with damping model B. In the case of small damping with Model A, no vortices were observed.

This can be understood in such a way that, even though both damping models loose exactly the same amount of particles, model B removes energy faster due to the loss of particles with higher kinetic energy.

For systems with a time dependent potential higher k-values get excited over time so that the influence of the k-dependent damping becomes stronger due to a greater overlap of the wave function in k-space and the damping potential.
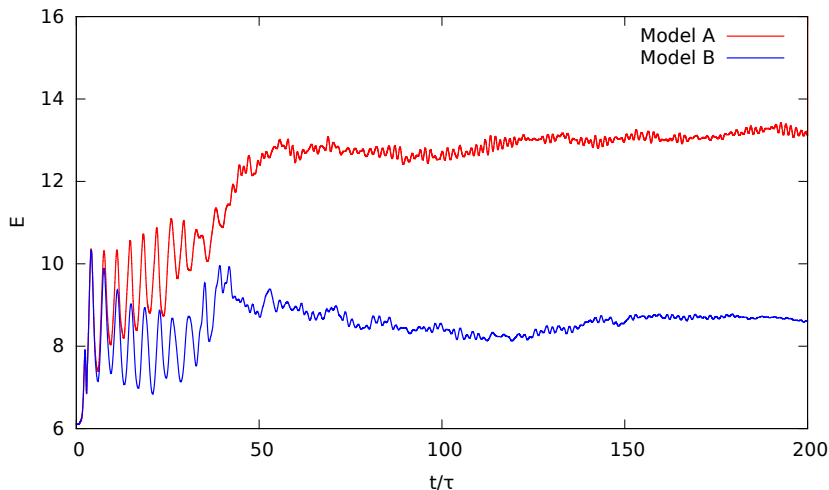
Figure 10: Energy. Same parameters as in figure 2, except for a smaller $\gamma_A = 2 \times 10^{-9}$ and parameters for model B as described in figure 5.3.3. It can be seen that a γ_A that creates the same loss of particles results in a high gain of energy and diffusion of the condensate.

5.4   Parameter Choice

The relation between k_0 and the healing length $k_0 = \frac{2\pi}{6\xi} \approx 5$, presented in equation (27) was found out empirically, by running simulations with varying damping parameters and comparing the results.

It was obvious that k_0 should be smaller than the k-value corresponding to the edges of the simulation box in k-space $k_0 > \frac{2\pi}{\Delta x}$ for a certain step size in real space Δx. If k_0 is on

the other hand chosen too low $k_0 = \frac{2\pi}{6.5\,\xi} \lesssim 4$, higher excitations that would have caused vortices will be damped too fast.

Even though this effect could be compensated by choosing a smaller γ_B, a larger k_0 is favourable, because then γ_B can be used to tune the loss of particles. When k_0 is set to a specific value by using equation (27), a value of $\gamma_B \approx 0.01$ turned out to be a good starting point.

On the other hand, it turned out that with higher k_0 the simulation does not yield stationary states as fast, especially if a step function is chosen instead of a smoother damping function.

The effect of improperly chosen parameters is shown exemplary in figure 11. The upper graph shows the time evolution of the angular momentum for the parameters chosen for the simulations before. The second graph shows the effect of a large k_0. Even though vortices are created, it takes the simulation longer to stabilise. The third and fourth graph show simulations where no vortices were created, by either a too small k_0 or too large γ_B, respectively.
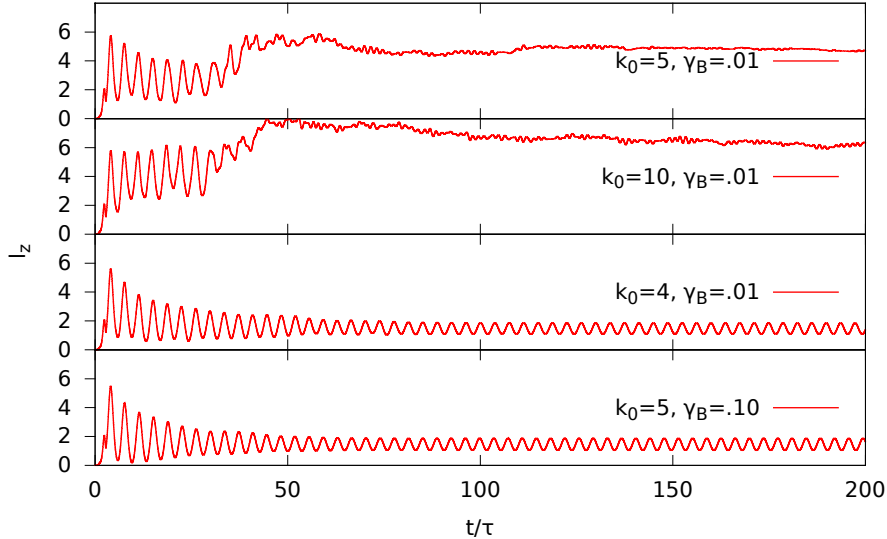
Figure 11: Angular momentum for different damping parameters. The first graph corresponds to a simulation with correctly chosen k_0 and γ_B. When k_0 is chosen too large (second graph), the system will not stabilise as fast, but if chosen too low higher excitations are hindered (third graph). The last graph shows that also a simulation with too high γ_B does not show vortices as well.

18

5.5 Effect of Quartic Potential

It has already been stated, that quadrupole excitations are needed to create vortices in BECs in a rotating trap. These modes are naturally excited by a trapping potential like

$$\hat{V}_{x^4}(\mathbf{r}, t) = c_4 \frac{1}{2} \left((1 + \varepsilon)^2 \, \tilde{x}^4 + (1 - \varepsilon)^2 \, \tilde{y}^4 \right) \tag{35}$$

with $\tilde{x} = x \cos(\Omega t) - y \sin(\Omega t)$ and $\tilde{y} = x \sin(\Omega t) + y \cos(\Omega t)$.[3]. The parameter c_4 is the strength of the quartic potential that will be added to the harmonic trap from equation (34).

The effect of the additional quartic potential on the trapping potential can be seen in figure 12. In this plot, the black lines are isolines of the original external potential of the simulations done before. These are compared with isolines of potentials with different quartic fractions. The quartic part results in a relative strengthening of the potential along the main axes.
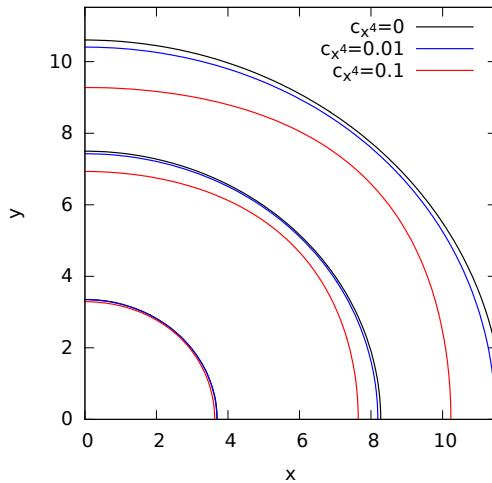
Figure 12: Isolines of $V(\mathbf{r}, 0)$ for different quartic potential strengths c_4 with the potential used for the simulation in figure 5. The function values of the isolines are 0.2, 1 and 2. It can be seen that the additional quartic potential adds just a small deformation.

It is clear, that a simulation with high quartic potential fraction excites the quadrupole mode to a greater extend, so that vortices should be created faster. This behaviour can be seen in figure 13, where the time evolution of the angular momentum of simulations with different quartic potential fractions are compared. A purely quadratic potential takes about 40 rotations, whereas a simulation with a c_4 of 0.01 creates the first vortex after less than 10 rotations.

For a large quartic potential fraction c_4 no scissors mode was observed. Instead, vortices began to collocate on the borders and entered the condensate simultaneously within the first 10 rotations.
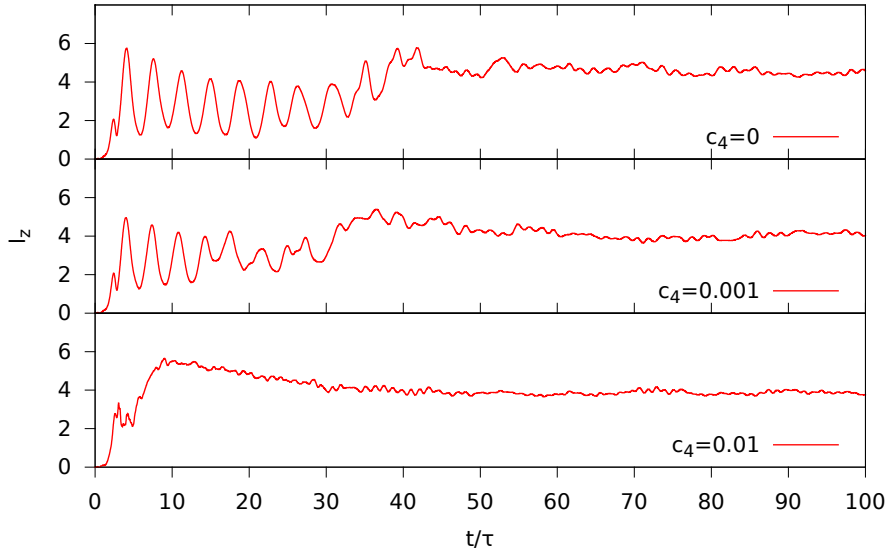
Figure 13: Time dependency of the angular momentum for different quartic potential strengths c_4. All other parameters were kept exactly the same as for the simulations in section 5.3.3. It can be seen that a potential strength of 0.001 did slightly accelerate the creation of vortices. For $c_4 = 0.01$ vortices were created within the first 10 rotations and stabilised extremely fast.

5.6 Dynamics of Vortex Creation

This chapter will give an insight into the dynamics of the creation of vortices depending on the rotation frequency of the trap. Two systems with different coupling constants g were simulated using damping model B. The quadratic trapping potential was rotated with frequency Ω, which was turned on linearly within 3τ and held constant afterwards.

To investigate the dynamics of the trapped BEC, several simulations with different maximum rotational frequencies were performed, which allowed an estimation of the critical rotational frequency. The results of the critical frequency were compared to equation (12) which uses the Thomas-Fermi approximation that only holds for large g.

5.6.1 g=25

The first set of simulations was performed for $g = 25$ with $k_0 = 2.5$ according to the estimate $k_0 = 2\pi/6\,\xi$ from equation (27) and $\gamma_B = 0.01$. The chemical potential $\mu = 3.01$ was found by propagating the system in imaginary time and measuring the change of normalisation. By inserting μ into equation (12), one gets a critical rotation frequency of $\Omega_{TF} = 0.56$.

The results of the simulation at $t = 200\tau$ are shown in figure 14. It can be seen that for small $\Omega < 0.7$ the asymmetry of the condensate increases with increasing Ω. For $\Omega = 0.7$ the density shows two vortices at the edge of the condensate. The critical velocity for which a vortex enters the condensate was found to be $\Omega_c \approx 0.725$, which is 30% higher than the value obtained from the Thomas-Fermi limit due to the comparatively small g. From this critical frequency on, an increase in Ω yielded an increase in the number of vortices.
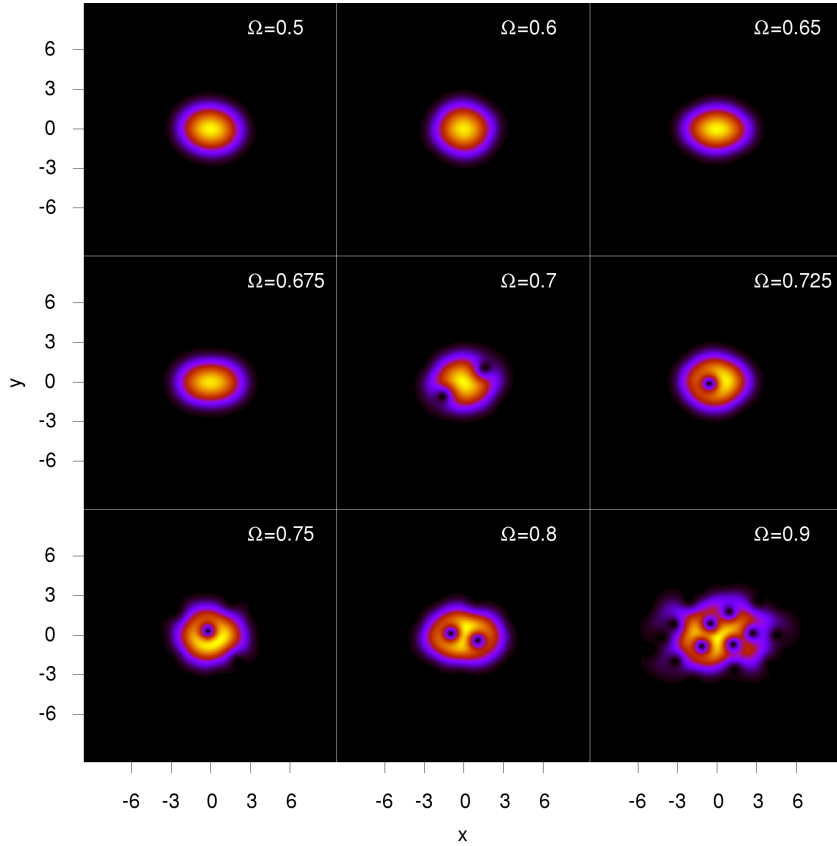
Figure 14: Density of the wave function at $t = 200\tau$ with k-dependent damping for different rotational frequencies. The simulation parameters were: $\Delta t = 0.0025$, $g_{2D} = 25$, $\omega_x = 0.95$ and $\varepsilon = 0.0975$. According to the estimation $k_0 \approx \frac{2\pi}{6\xi}$, k_0 was set to 2.5 and $\gamma_B = 0.01$. The estimated critical frequency for this system is $\Omega_c \approx 0.725$, which is higher than the theoretical value of $\Omega_{TF} = 0.56$.

A good way to show the dynamics of the system is to compare the time evolutions of the angular momenta, which is done in figure 15. In the case of $\Omega = 0.65$, only a small elliptic deformation of the condensate can be seen which adds only little angular momentum.
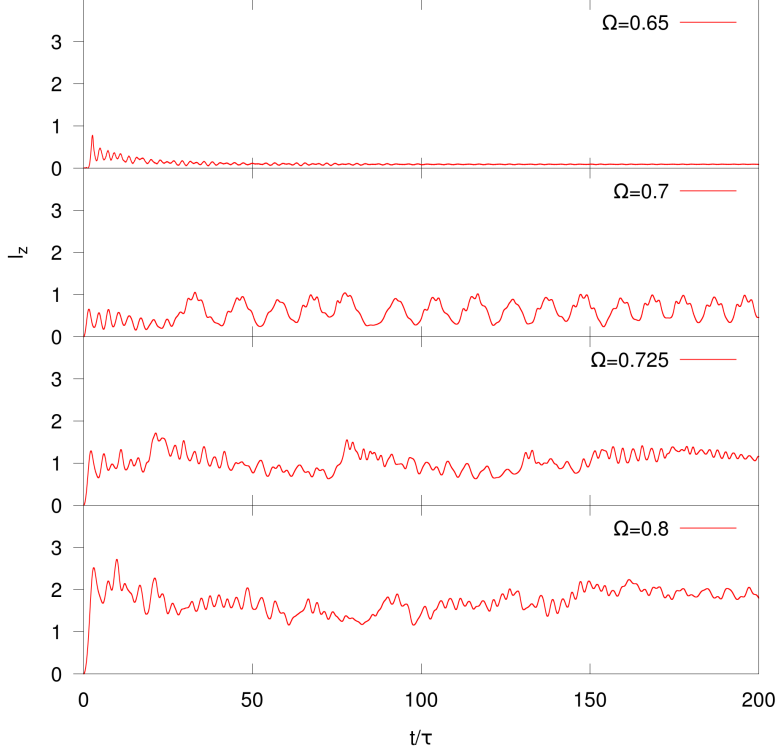
Figure 15: Angular momentum for the simulation described in figure 14. For $\Omega = 0.7$, which was the case with two vortices on the outside of the condensate, strong oscillations in the angular momentum were observed. These oscillations correspond to two vortices which periodically enter opposed edges of the condensate. The simulation for $\Omega = 0.725$ resulted in a single-vortex state.

In the case of $\Omega = 0.7$ an oscillation of the angular momentum between 0 and 1 was observed, whose origin will be shown in detail. For the critical velocity $\Omega = 0.725$ the equilibration of the system into a vortex state with $l_z = 1$ can be seen after $t = 170\tau$. For $\Omega = 0.8$ the angular momentum converged to a value of 2 when the stable state shown in figure 14 was reached after $t = 160\tau$.

Figure 16 shows how a vortex entered the BEC for $\Omega = 0.725$. The vortices on the edge of the condensate came closer over time until one vortex entered the condensate and slowly spiralled inwards.
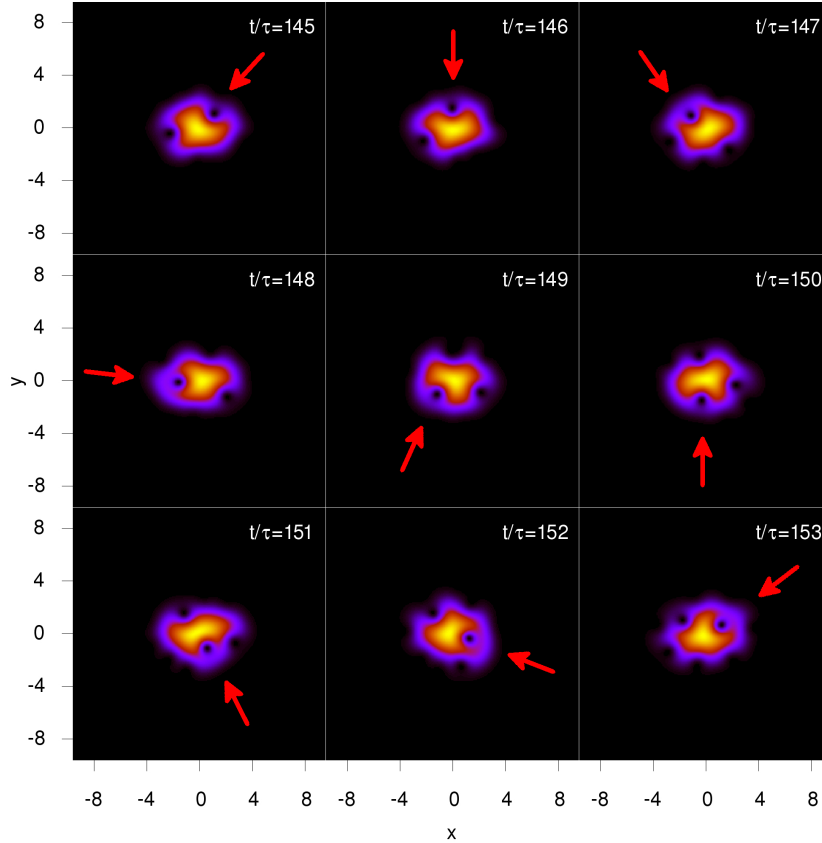
Figure 16: Time evolution of the density of the wave function for the simulation with $\Omega = 0.725$ described in figure 14. It can be seen that the vortex marked with a red arrow slowly spiralled inwards.

The angular momentum for the simulation $\Omega = 0.7$ showed an interesting pattern. In figure 17 the density of the condensate was plotted for different points in time during these oscillations. The red and blue arrows mark pairs of vortices that move in and out of the edges of the condensate periodically. At $t = 52\tau$ the angular momentum is at a minimum where the four vortices have the same distance from the center of the cloud. When the red marked vortices then enter the condensate until $t = 58\tau$ the angular momentum increases to 1 and likewise decreases when they leave again. This process is then repeated with the blue vortices from $t = 62\tau$ on.

Other kinds of oscillatory behaviour in the angular momentum can be seen in simulations where $\Omega > \Omega_c$. As an example, the time evolution of the simulation with $\Omega = 0.725$ is shown at $t = 50\tau$ in figure 18. Two vortices, that lay on opposite sides of the condensate and circle around it can be seen. The frequency of this oscillation is higher than in the previously mentioned case of $\Omega = 0.7$.
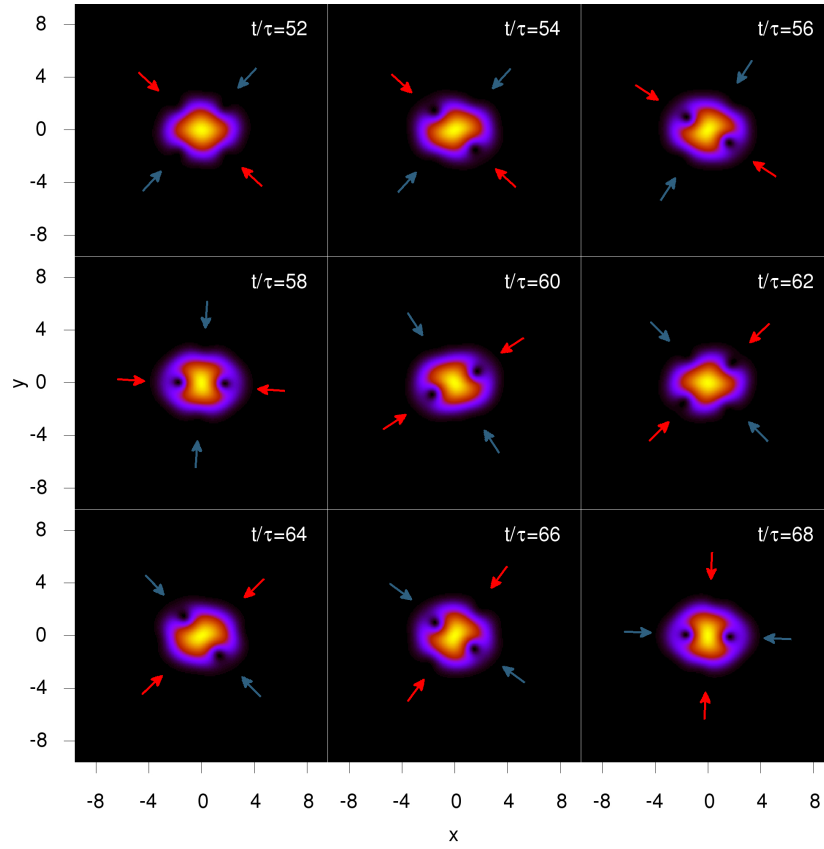
Figure 17: Time evolution of the density of the wave function for the simulation with $\Omega = 0.7$ described in figure 14. The red and blue arrows mark the positions of vortices that enter and leave the edges of the condensate periodically.
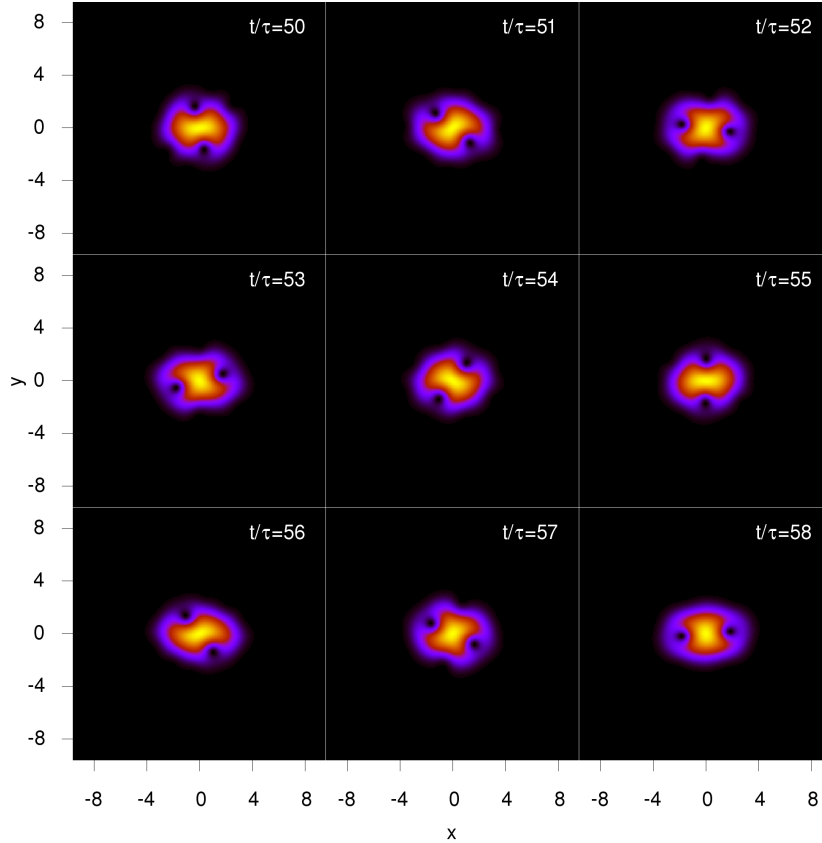
Figure 18: Time evolution of the density of the wave function for the simulation with $\Omega = 0.725$ described in figure 14. Two vortices, that circle around the edges of the condensate can be seen. Compared to figure 17, a larger Ω results in a oscillation with higher frequency.

5.6.2   g=250

The same procedure as in section 5.6.1 was also carried out with a coupling constant of $g = 250$, $\gamma_B = 0.01$ and $k_0 = k$ in accordance with equation (27). The density after 200 rotations and time dependency of the angular momentum for different rotation frequencies are plotted in figures 19 and 20, respectively.

In the simulations a critical velocity of $\Omega_c = 0.50$ was found, which is higher than the value $\Omega_{TF} = 0.31$ in the Thomas-Fermi limit. Due to similar parameters as in the simulation of Madison et al., the density for the frequency $\Omega = 0.7$ looks similar to the vortex lattice shown in figure 5.

The time dependency of the simulations with $g = 250$ look very similar to each other, which can be seen for example in the angular momentum which oscillates with a high frequency in all cases. A typical time dependency of the motion of the condensate during these oscillations in the angular momentum can be seen in figure 21. It shows that the condensate gets an elliptic shape which is rotated relatively to the axes of the potential.

25

In comparison to the simulations with lower g shown in figure 17, more density fluctuations were found on the edges of the condensate within the first 50 rotations of the trap. Due to the smaller healing length compared to $g = 25$ the vortices are able to lie closer to each other. However, the oscillatory behaviour shown in figure 17 was not observed. Like in figure 16, the vortex entered the condensate from the outside which can be seen in figure 22. Compared to the simulation with $g = 25$ the inward motion of the vortex is much slower.
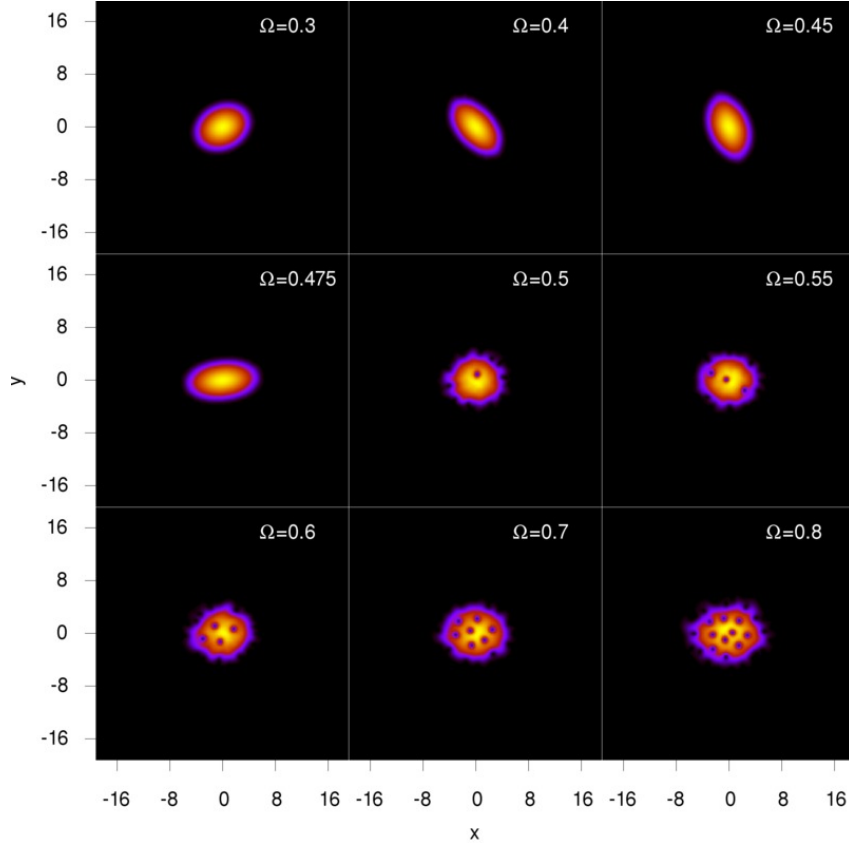
Figure 19: Density of the wave function after 200 rotations with k-dependent damping for different rotational frequencies. The parameters were: $\Delta t = 0.001$, $g_{2D} = 250$, $\omega_x = 0.95$ and $\varepsilon = 0.0975$. According to the estimation $k_0 \approx \frac{2\pi}{6\xi}$, k_0 was set to 5 and $\gamma_B = 0.01$. The critical frequency was found to be $\Omega_c = 0.5$
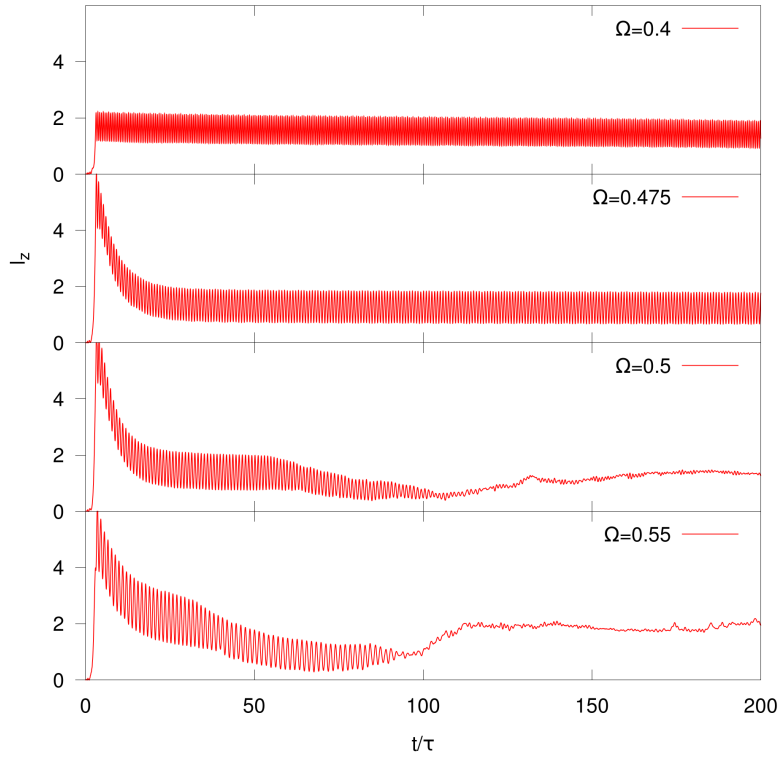
Figure 20: Angular momentum for the simulations described in figure 19. It can be seen that the rotation excites modes with high frequencies in all cases. In the simulation with $\Omega = 0.5$, the vortex enters the condensate at $t = 100\tau$.
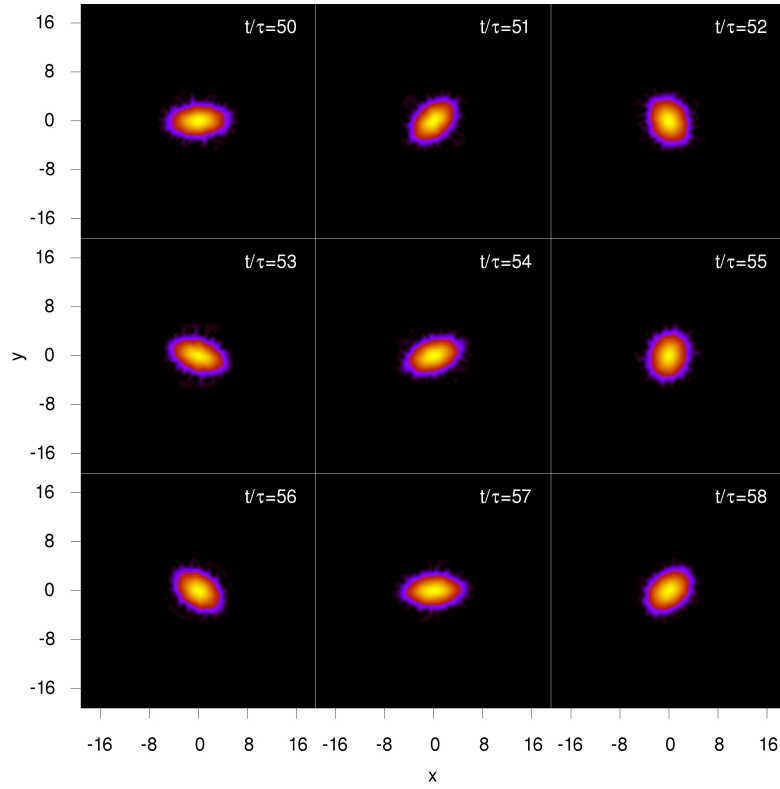
Figure 21: Time dependency of the density for the simulation with $\Omega = 0.5$. The oscillations that are visible in the angular momentum correspond to elliptic shape deformations.
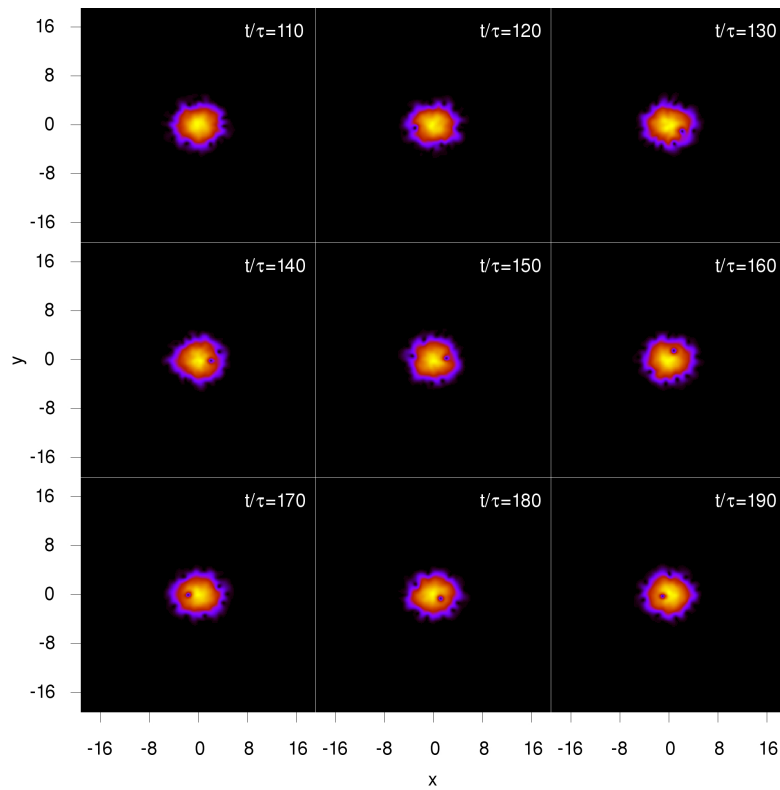
Figure 22: Time evolution of the density for the simulation with $\Omega = 0.5$ described in figure 14. It can be seen that the vortex spirals inwards slowly.

6 Toroidal Bose–Einstein Condensates

In this section, the effect of damping models A and B on the simulations of stirred toroidal BECs will be treated. Recently, a paper by Eckel et al. showed discrepancies between simulations of the GPE using damping model A and the corresponding experiment [8]. The goal is to investigate whether the simulation results differ for damping model A or B and whether model B leads to better agreement with the experiment.

The toroidal shape of the condensate was created by a static harmonic potential along the radial direction centered around a certain radius R:

$$\hat{V}_{static}(\mathbf{r}) = \frac{1}{2}m\,\omega_\perp^2 \left(\sqrt{x^2 + y^2} - R \right)^2 \tag{36}$$

The unit system will be defined like in equation (40), with the oscillator length of the harmonic potential along the radial direction $x_0 = \sqrt{\hbar/m\,\omega_\perp}$, the mass of the atoms m and the trap frequency $\omega_\perp$ along the radial direction:

$$x' = x/x_0 \tag{37}$$

$$E' = E/\left(\hbar\,\omega_\perp\right) \tag{38}$$

$$g' = g/\left(\frac{\hbar^2}{m}x_0\right) \tag{39}$$

$$\Omega' = \Omega/0.01\,\omega_\perp \tag{40}$$

As time scale the quantity $\tau = 2\pi/\Omega_0$ will be used.

The prefactor in the definition of Ω' is motivated by a different choice in reference length compared to the experiment of Eckel et al. . In our system, the reference is the oscillator length x_0 compared to $R = 10\,x_0$ in the case of Eckel et al. By choosing the reference length as Eckel, a reference frequency of $\Omega_0 = \hbar/mR^2$ arises. This frequency is linked to the trap frequency via

$$\Omega_0 = \frac{\hbar}{m\left(10\,x_0\right)^2} = 0.01\,\omega_\perp \tag{41}$$

so that $\Omega' = \Omega/\Omega_0 = \Omega/\omega_\perp\,0.01$ follows.

The radius was chosen so that the shape of the ground state density of the BEC roughly matches the shape of the experimentally found ground state density of Eckel et al. This

length was also chosen by Piazza et al. for their numerical investigation of the critical velocity of a toroidal BEC [19].

Figure 23 shows the ground state of this trap for $g = 700$ and $R = 10$ with the oscillator length x_0 found by 500 imaginary time propagation steps.
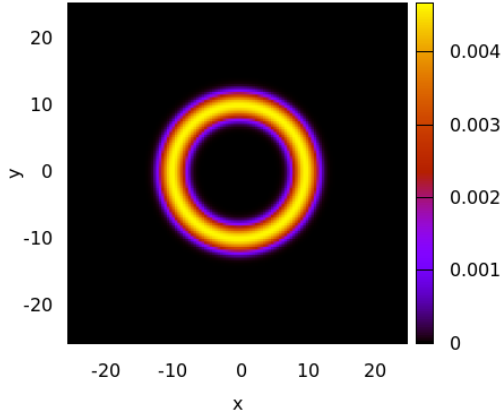
Figure 23: Ground state density. The radius $R = 10$ of the condensate was chosen to be comparable with Eckel et al. [8]. The parameters were: $g = 700$, $\Delta t = 0.01$.

In addition to the static potential, a time dependent Gaussian potential along the azimuthal direction was used to stir the condensate by creation of a rotating weak link. Hence, the full external potential had the form

$$\hat{V}(\mathbf{r}, t) = \frac{1}{2}(\sqrt{x^2 + y^2} - R)^2 + \Theta(\tilde{x})\, U(t)\, \mu \exp\left(-\tilde{y}^2/2\,\sigma^2\right)/\sqrt{2\pi\,\sigma^2} \qquad (42)$$

with $\tilde{x} = x\cos(\Omega t) - y\sin(\Omega t)$, $\tilde{y} = x\sin(\Omega t) + y\cos(\Omega t)$, the Heaviside function $\Theta(\tilde{x})$ and the variance of the Gaussian $\sigma = 0.5$. The potential strength is determined by the function $U(t)$.

By stirring the BEC with $\Omega \neq 0$, a phase jump along the azimuthal direction can be induced when the stirring frequency is larger than a critical frequency $\Omega \geq \Omega_c^+$. To loose this phase jump again, the stirring frequency may be even lower than Ω_c^+. The frequency at which the phase jump is lost again will be called Ω_c^-. The difference in these critical stirring frequencies was experimentally investigated and calculated by Eckel et al. in 2014 [8].

6.1 Experiment and Calculations of Eckel et al.

The experimental procedure by Eckel et al. that can be seen in figure 24 consisted of two steps. The first step prepared the previously equilibrated BEC in a state with either $l_z = 0$ or $l_z = 1$ by rotating the potential with $\Omega = 0$ (dashed blue curve) or $\Omega = \Omega_1$ (red curve), respectively. Here, Ω_1 was fixed to a value greater than Ω_c^+ so that the outcome using this frequency was always a state with $l_z = 1$. The potential strength of the rotating potential was turned on linearly, held constant at U_1 and turned off linearly afterwards (green curve).

The next step was the actual measurement. The same procedure as before was done, but with a different potential strength U_2 and frequency Ω_2. Depending on the previously prepared state, the rotation could induce a phase jump, annihilate a phase jump or neither of the two. When the BEC was originally prepared in the state $l_z = 0$, a phase jump could only be induced when $\Omega_2 > \Omega_c^+$. Likewise, for $l_z = 0$, a phase jump could only be destroyed for $\Omega_2 < \Omega_c^-$.
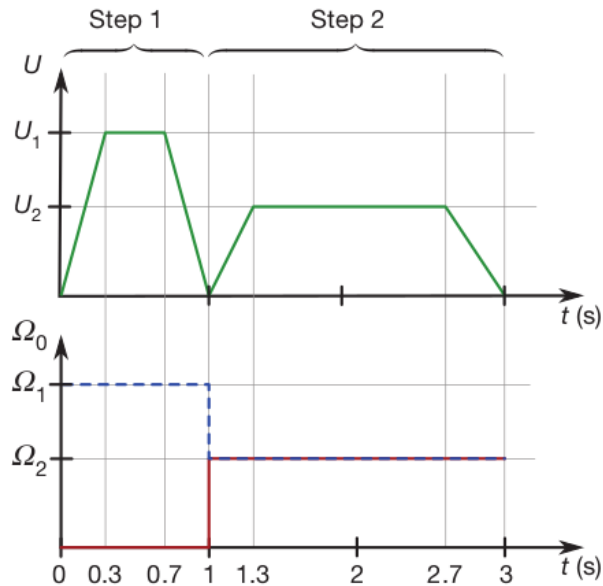
Figure 24: Experimental procedure of the experiments by Eckel et al. The first step prepares the BEC in either a state with $l_z = 1$ or $l_z = 0$ depending on the chosen Ω_1. In the second step, the same procedure was repeated with varying rotating potential strength U and rotational frequency Ω_2 to test whether a phase jump was lost or induced. Image taken from reference [8].

To get the exact critical frequencies for a certain U_2 several experiments with varying Ω_2 were performed. The resulting angular momentum was averaged over 20 experiments and plotted over Ω_2. A hysteresis curve could then be fitted to determine Ω_c^+ and Ω_c^-.

In figure (25) the hysteresis width $\Omega_c^+ - \Omega_c^-$ depending on the potential strength U_2 is plotted. Notice, that by defining the unit system as before, the reference frequency Ω_0 defined in equation (41) equals 1.

Not only the experimental results, but also the results for calculations of this setup by Eckel et al. are plotted. The green dots show the experimental data with uncertainties, the magenta line is the prediction of an effective one-dimensional hydrodynamic model with corresponding uncertainty shown as magenta band and the cyan diamonds show the results of GPE simulations in the laboratory frame using damping model A with either $\gamma_A = 0$ (open) or $\gamma_A = 0.01$ (filled).

It can be seen, that all of the calculations yielded a much greater hysteresis width than the experiment. However, for large rotating potential strengths the loop width $\Omega_c^+ - \Omega_c^-$ approaches 0 in all cases.

This discrepancy raises the question, whether a better damping model, e.g. model B, improves the result of the simulations or if there is no difference between model A and B. To do so, a stirred toroidal BEC will be simulated for two different coupling constants g and varying potential strengths to test whether damping models A and B yield different critical frequencies.
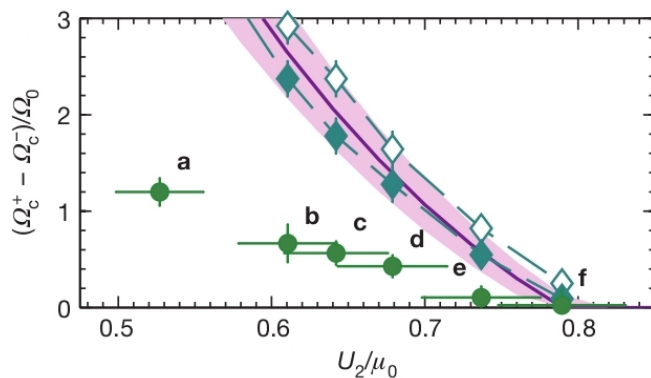
Figure 25: Hysteresis width of the experiments of Eckel et al. depending on the rotating potential strength. In our reduced units and by defining the potential as in equation (42) the quantities have to be interpreted as $\left(\Omega_c^+ - \Omega_c^-\right)/\Omega_0 \mapsto \Omega_c^+ - \Omega_c^-$ and $U_2\,\mu_0 \mapsto U_2$. The green dots show the experimental data, the magenta line shows the results of an effective one-dimensional hydrodynamic model with uncertainty shown as magenta band. The diamonds show the results of GPE simulations using either $\gamma_A = 0$ (open) or $\gamma_A = 0.01$ (filled). Image taken from reference [8].

6.2 Simulations

In contrast to the experiment of Eckel, a different precedure was used in order to test the critical frequencies for a certain U and g within one simulation. First, the wave function

was prepared to be in the ground state of the trap via 500 imaginary time steps. Then the potential strength was turned on linearly within $\Delta t/\tau = 0.2$ to $U = U_0$ and held constant afterwards, as shown in figure 26. During this step, the weak link was created. Notice, that the abscissa for the abscissa in figure 26 was magnified tenfold from -0.2 to 0. Then, to induce angular momentum, Ω was turned on with a slope of $(\Delta\Omega/\Delta(t/\tau) = 0.1)$.

When the first phase jump along the radial direction was observed by directly plotting the phase along the line $\sqrt{x^2 + y^2} = R$ the critical frequency Ω_c^+ was reached. This event is marked as green dash-dotted line in the time scale, while Ω_c^+ is shown as green dashed line. The effect of the phase jump can be seen in the angular momentum which peaked to a value of $l_z = 1$.

Next, the rotational frequency was held constant at Ω_c^+ within $\Delta t = 2\pi/\Omega_c^+$, shown as shaded area, to give the system time to equilibrate. Then Ω is decreased with the same slope as before until the phase jump is lost again, which marks Ω_c^-. At this point, also the angular momentum drops down to a value far below 1. The critical frequency and the time when it was reached are shown as blue dashed and dash-dotted lines, respectively.
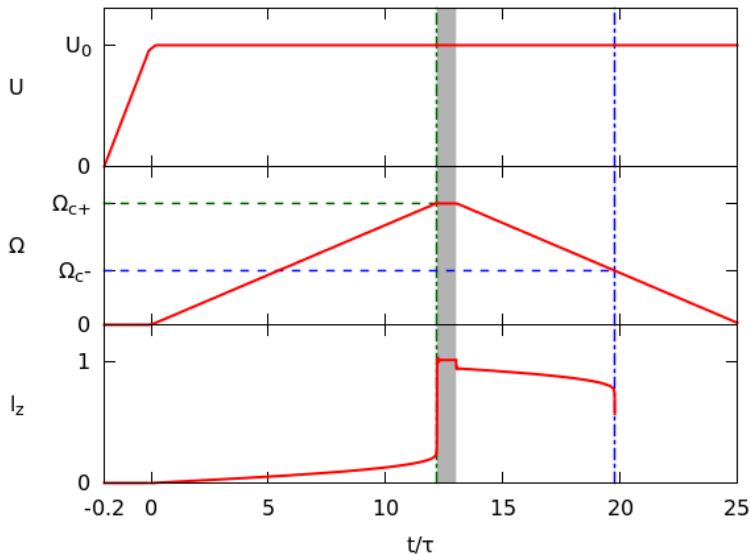
Figure 26: Schematic setup of the simulations. Note, that the abscissa is magnified tenfold until $t/\tau = 0$. The potential strength U was turned on linearly within $\Delta t = 0.2\tau$. Then the rotational frequency Ω was ramped up linearly with rate $\Delta\Omega/\Delta(t/\tau) = 0.1$ until a phase jump was induced at $\Omega = \Omega_c^+$. Then, Ω was held constant (shaded area) to give the system time for equilibration, before Ω was ramped down again with the same slope as before. The phase jump was lost when the second critical frequency Ω_c^- was reached. The third plot shows that the angular momentum jumps to 1 when the phase jump was induced, and drops significantly when it was lost again.

6.2.1 g=700

First, simulations with $g = 700$ were performed using either damping model A with $\gamma_A = 0.01$ or damping model B using $k_0 = 2.5$ and $\gamma_B = 0.01$. The estimation of k_0 was based on equation (27) with $\mu = 3.3$. The ground state for this simulation has already been shown in figure 23.

Figure 27 shows the density of the BEC plotted along the line with radius $r = R = 10$, i.e. the line where the potential is at its minimum, after switching on U before the rotation starts for different potential strengths. It can be seen that the depletion of the BEC varies over a broad range, so that a broad Ω range was covered with the simulations.
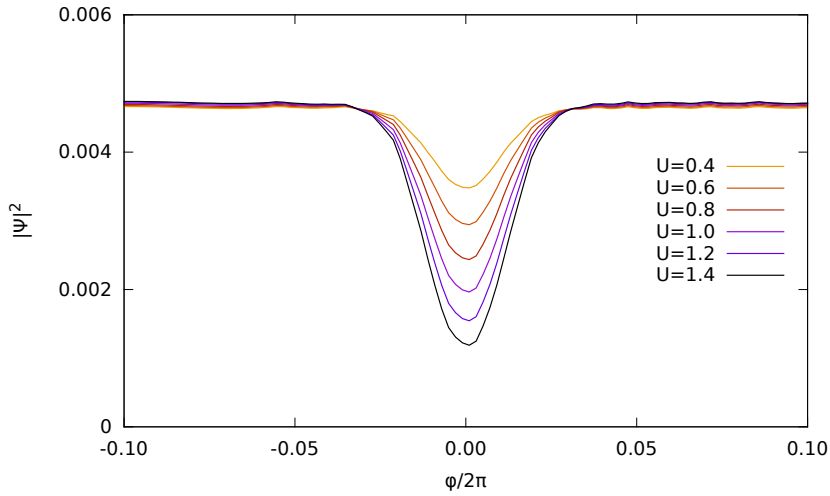
Figure 27: Density of the condensate along the line $\sqrt{x^2 + y^2} = R = 10$. The parameters were: $g = 700$, $\Delta t = 0.01$. This plot shows how the rotating potential alters condensate when turned on fully for different U.

The critical frequencies estimated from simulations using damping model A or B are shown in figure 28. Here, the upper and lower curves correspond to Ω_c^+ and Ω_c^-, respectively. Even though a similar hysteresis behaviour was observed, no significant differences in the $\Omega_c^\pm$ were observed between damping models A and B. This can be also seen in figure 29 that shows the hysteresis width, which can be directly compared to figure 25. A similar behaviour was observed, even though the g value was chosen randomly.
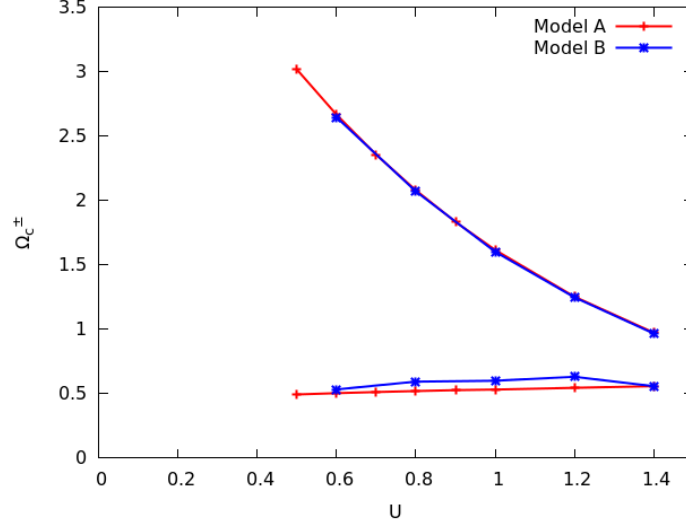
Figure 28: Critical rotational frequencies for various potential strengths. The parameters were: $g = 700$, $\Delta t = 0.01$. The upper two curves and lower two curves in this plot correspond to Ω_c^+ and Ω_c^-, respectively. The simulations were performed using damping model A with $\gamma_A = 0.01$ and model B with $k_0 = 2.5$ and $\gamma_B = 0.01$. No significant difference in the observed critical frequencies for damping model A and B can be seen.
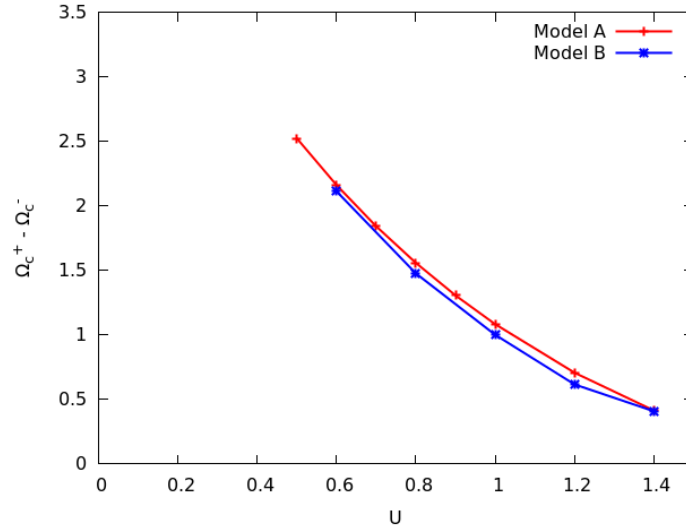
Figure 29: Hysteresis loop size for various potential strengths, using the data in figure 28.

6.2.2   g=2000

The same procedure as before was repeated with $g = 2000$ to test, whether a different result could be achieved. For damping model B, γ_B was set to 0.01 and $k_0 = 5$ was estimated using equation (27) with $\mu = 6.5$.

The ground state density of the BEC after imaginary time propagation is shown in figure 30 and the density along the line $\sqrt{x^2 + y^2} = R = 10$ can be seen in figure 31.
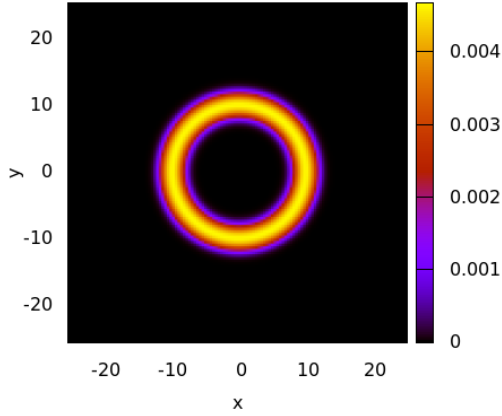
Figure 30: Ground state density of the condensate. The parameters were: $g = 2000$, $\Delta t = 0.005$.
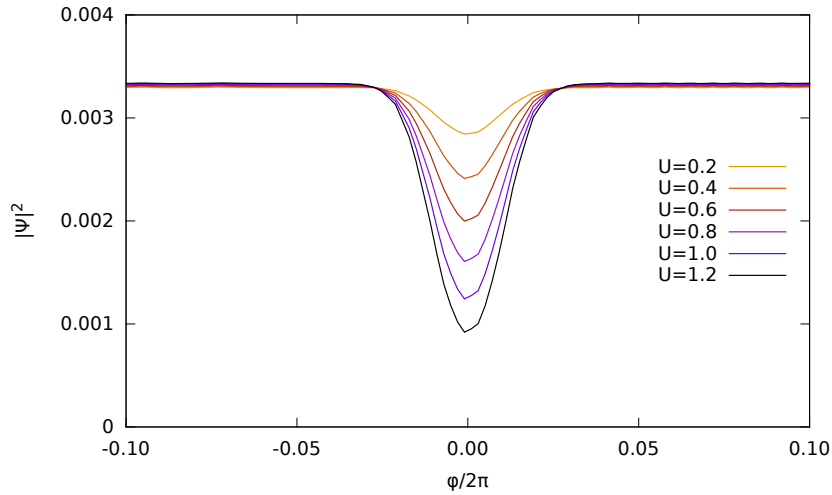
Figure 31: Density of the condensate along the line $\sqrt{x^2 + y^2} = R = 10$. The parameters were: $g = 2000$, $\Delta t = 0.01$. This plot shows how the rotating potential alters condensate when turned on fully for different U.

Figures 32 and 33 show the estimated critical rotational frequencies and the hysteresis loop size, respectively. As in the case of $g = 700$, no significant difference between models A and B can be seen, which leads to the conclusion that in this type of simulation, damping model B does not yield any further improvement.
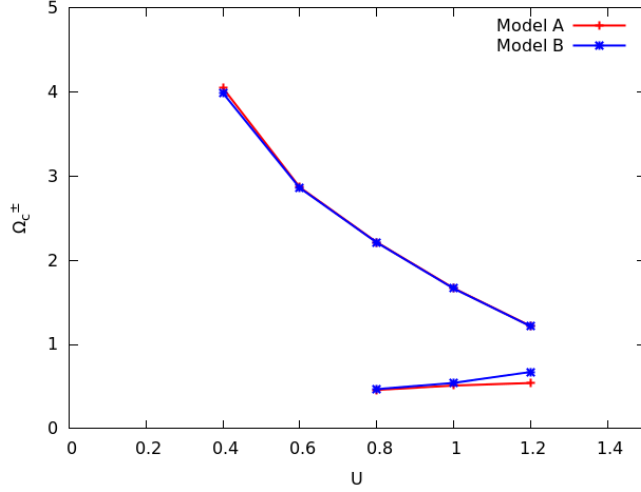
Figure 32: Critical rotational frequencies for various potential strengths. The upper two curves and lower two curves in this plot correspond to Ω_c^+ and Ω_c^-, respectively. The simulations were performed using damping model A with $\gamma_A = 0.01$ and model B with $k_0 = 5$ and $\gamma_B = 0.01$. No significant difference in the observed critical frequencies using damping model A and B can be seen. The parameters were: $g = 2000$, $\Delta t = 0.01$.
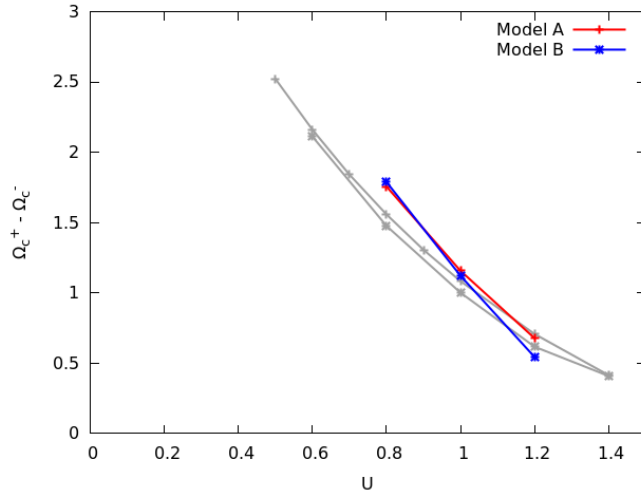
Figure 33: Hysteresis loop size for various potential strengths, using the data in figure 32. The hysteresis loop size for $g = 700$ shown in figure 29 is plotted in grey.

Compared to the experiment and calculations of Eckel et al. in figure 25, the hysteresis size in figure 33 decreases to 0 slower. From the trend, that a higher g results in a greater hysteresis loop width it may be followed, that either the g value that describes the system of Eckel et al. is lower than 700. However, also the arbitrary choice of R and a different definition of the rotating potential may be the reason for discrepancies.

Even though the experiment was not directly comparable with our simulation data, it was found out that there is no difference in the resulting critical frequencies for damping model A and B in the treated cases.

7 Conclusion

It was found out that the momentum-dependent damping model B showed several advantages over the commonly used damping model A. By using damping model A in the rotating frame of reference, the BEC would always be damped into the ground state under rotation, which would not have shown the correct dynamics. For this reason, the calculations were performed in the laboratory frame. When simulating a BEC in a harmonic trap under rotation model A did not predict the onset of vortices, even though simulations with model B were able to describe the dynamic creation of vortices accurately so that the dynamics of the experiment of Madison et al. [5] could be reproduced.

Using damping model B, we investigated the dynamic creation of vortices and the necessity of quadrupole excitations for them to enter the condensate. It was shown, that the first vortex that enters the condensate rotated with the critical frequency spirals inward for two different coupling constants. A regular pattern of vortices oscillating in and out of the BEC was observed for a small g just below the critical rotation frequency. Though, for larger g the dynamics were more diffuse due to a denser arrangement of vortices along the edges of the BEC.

Lastly, damping models A and B were tested on stirred toroidal BECs, where a discrepancy between the experimental and simulation results in the critical stirring frequencies was found by Eckel et al. , Even though, damping model B was better suited to describe BECs in harmonic traps, it yielded the same results as model A, which leads us to the conclusion that it does not agree with the experimental results of Eckel et al. either.

References

[1] Ryan M. Wilson et al. "Manifestations of the roton mode in dipolar Bose-Einstein condensates". In: *Physical Review Letters* 100.24 (2008).

[2] R. Kishor Kumar and P. Muruganandam. "Vortex dynamics of rotating dipolar Bose-Einstein condensates". English. In: *Journal of Physics B* 45.21 (2012).

[3] L. Pitaevskii and S. Stringari. *Bose-Einstein Condensation*. Clarendon Press, 2003.

[4] J. R. Abo-Shaeer et al. "Observation of vortex lattices in Bose-Einstein condensates". In: *Science* 292.5516 (Apr. 2001), pp. 476–479.

[5] KW Madison et al. "Stationary states of a rotating Bose-Einstein condensate: Routes to vortex nucleation". In: *Physical Review Letters* 86.20 (2001), 4443–4446.

[6] M. R. Matthews et al. "Vortices in a Bose-Einstein condensate". In: *Physical Review Letters* 83.13 (Sept. 1999), pp. 2498–2501.

[7] M Tsubota, K Kasamatsu and M Ueda. "Vortex lattice formation in a rotating Bose-Einstein condensate". English. In: *Physical Review A* 65.2 (2002).

[8] S. Eckel et al. "Hysteresis in a quantized superfluid 'atomtronic' circuit". In: *Nature* 506 (2014), p. 200.

[9] EP Gross. "Structure of a quantized Vortex in Boson Systems". English. In: *Nuovo Cimento* 20.3 (1961), 454+.

[10] LP Pitaevskii. "Vortex Lines in an Imperfect Bose Gas". English. In: *Soviet Physics JETP-USSR* 13.2 (1961), 451–454.

[11] C. J. Pethick and H. Smith. *Bose-Einstein Condensation in Dilute Gases*. Cambridge University Press, 2002.

[12] M. Cozzini et al. "Scissors mode of a rotating Bose-Einstein condensate". In: *Physical Review A* 67.2, 021602 (Feb. 2003), p. 021602.

[13] D. Guéry-Odelin and S. Stringari. "Scissors Mode and Superfluidity of a Trapped Bose-Einstein Condensed Gas". In: *Physical Review Letters* 83 (22 1999), pp. 4452–4455.

[14] E. Lundh, C. J. Pethick and H. Smith. "Zero-temperature properties of a trapped Bose-condensed gas: Beyond the Thomas-Fermi approximation". In: *Physical Review A* 55 (3 1997), pp. 2126–2131.

[15] S. A. Chin and CR Chen. "Gradient symplectic algorithms for solving the Schrodinger equation with time-dependent potentials". In: *Journal of Chemical Physics* 117.4 (2002), 1409–1415.

[16] S. A. Chin. "Higher-order splitting algorithms for solving the nonlinear Schrodinger equation and their instabilities". In: *Physical Review E* 76.5, 2 (2007), p. 056708.

[17] ML Chiofalo, S Succi and MP Tosi. "Ground state of trapped interacting Bose-Einstein condensates by an explicit imaginary-time algorithm". English. In: *Physical Review E* 62.5, B (2000), 7438–7444.

[18] S. Choi, S. A. Morgan and K. Burnett. "Phenomenological damping in trapped atomic Bose-Einstein condensates". In: *Physical Review A* 57 (5 1998), pp. 4057–4060.

[19] F. Piazza, L. A. Collins and A. Smerzi. "Critical velocity for a toroidal Bose-Einstein condensate flowing through a barrier". In: *Journal of Physics B* 46.9 (2013).